Black N/H-TiO$_2$ Nanoplates with a Flower-Like Hierarchical Architecture for Photocatalytic Hydrogen Evolution

Kaifu Zhang,[a] Wei Zhou,*[a] Lina Chi,[b] Xiangcheng Zhang,[a] Weiyao Hu,[a] Baojiang Jiang,[a] Kai Pan,[a] Guohui Tian,[a] and Zheng Jiang*[b]

A facile two-step strategy was used to prepare black of hydrogenated/nitrogen-doped TiO$_2$ nanoplates (NHTA) with a flower-like hierarchical architecture. In situ nitriding and self-assembly was realized by hydrothermal synthesis using tripolycyanamide as a N source and as a structure-directing agent. After thorough characterization, it was found that the hydrogenation treatment did not damage the flower-like architecture but distorted the anatase crystal structure and significantly changed the band structure of NHTA owing to the increased concentration of oxygen vacancies, hydroxyl groups, and Ti^{3+} cations. Under AM 1.5 illumination, the photocatalytic H$_2$ evolution rate on the black NHTA was approximately 1500 µmol g^{-1} h^{-1}, which was much better than the N-doped TiO$_2$ nanoplates ($\approx$ 690 µmol g^{-1} h^{-1}). This improvement in the hydrogen evolution rate was attributed to a reduced bandgap, enhanced separation of the photogenerated charge carriers, and an increase in the surface-active sites.

Introduction

Since the discovery of photoelectric catalytic water splitting on low-cost, nontoxic, and stable TiO$_2$ electrodes, various band-engineering strategies have been attempted to narrow the bandgap of TiO$_2$ to harvest a larger portion of solar energy in the visible light region.[1–8] Doping with transition metal and/or nonmetal ions, creating structure defects through hydrogenation, surface metallization, and hybridization with low-bandgap semiconductors have been used as effective strategies.[6, 7, 9–12] Among these methodologies, N doping has been considered as a promising solution because it can be used to extend the visible light absorption, it has desirable photocatalytic activity, and acceptable level of recombination of photogenerated charge carriers.[13–15] However, the nitriding of TiO$_2$ either requires sophisticated processes, suffers from decomposition during water splitting, or faces significant energy loss owing to the recombination of charge carriers at high N doping levels.[6, 13, 16–18] Co-doping of N with other appropriate elements may further improve the performance owing to synergistic effects, but careful selection of the co-dopant and optimization of the material structure is necessary.[9, 13]

Recently, Chen and co-workers demonstrated excellent visible-light photocatalytic performance in water splitting on black, electron deficient ■■ok?■■anatase nanoparticles, derived from the hydrogenation of TiO$_2$, which opens up new possibilities for tuning of the TiO$_2$ band structure.[19] A few methods have been adopted for the synthesis of black TiO$_2$ materials,[20–25] but not many have been used to fabricate hierarchical architectures.[7, 26, 27] The exact working mechanism of the black TiO$_2$ is also under debate.[28] Moreover, the reported black TiO$_2$ materials possess limited stability owing to the loss of structure vacancies or structure-entrapped free-charges by adsorbed impurities.

Preferential exposure of the reactive surface of TiO$_2$ is another attractive route to maximize the photocatalytic activity of TiO$_x$ photocatalysts.[29, 30] Owing to their unique 2 D morphology, TiO$_x$ nanoplates would naturally contain large exposure of certain crystal facets and high surface areas, which would enable the tuning of the surface reactivity.[31] However, nanoplates are prone to aggregation to mitigate their extra surface energy and thus reduce the surface-active sites, unless they are fixed on a substrates or ensemble to constrain the oriental aggregation.

In this paper, we report the successful preparation of black hydrogenated/N-doped anatase TiO$_2$ nanoplates (hereafter NHTA) with a flower-like hierarchical architecture using a facile two-step strategy: hydrothermal synthesis followed by hydrogenation, in which tripolycyanamide serves as a N source and a self-assembly directing agent. The NHTA was explicitly investigated by thorough structural and spectral characterization. The photocatalytic hydrogen evolution rate on the black NHTA ($\approx$ 1500 µmol g^{-1} h^{-1}) was more than two times higher than that of the N-doped TiO$_2$ flower-like architecture (denoted as NTA) under AM 1.5 irradiation.

[a] K. Zhang, Prof. W. Zhou, X. Zhang, W. Hu, B. Jiang, K. Pan, G. Tian
Key Laboratory of Functional Inorganic Material Chemistry
Ministry of Education of the People's Republic of China
Heilongjiang University
Harbin 150080 (PR China)
E-mail: zwchem@hotmail.com

[b] L. Chi, Prof. Z. Jiang
Faculty of Engineering and the Environment
University of Southampton
Southampton, SO17 1BJ (United Kingdom)
E-mail: z.jiang@soton.ac.uk

Results and Discussion

Crystal structure and morphology

The XRD patterns of NHTA and NTA could be well indexed to an anatase phase (JCPDS, No.21-1272; Figure 1 A, $I4_1/amd$) The (101) diffraction (Figure 1 A inset) of NHTA was stronger and shifted to a slightly smaller 2θ compared to NTA, indicating that the hydrogenation gave rise to lattice strain and an in-
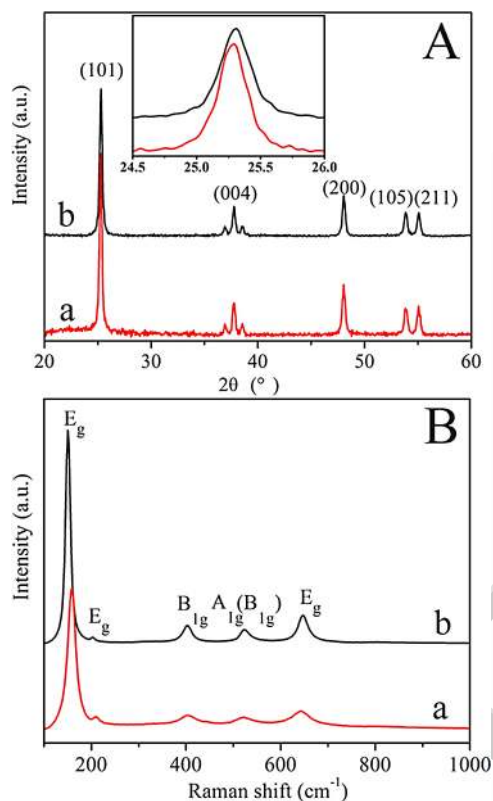

Figure 1. The (A) XRD patterns (B) and Raman spectra of (a) NHTA and (b) NTA. The inset is the amplified (101) XRD peaks.

creased crystallite size of anatase. As calculated from the (101) Bragg diffraction using the Scherrer equation, NHTA possessed larger average crystallite sizes (26.8 nm) than NTA (23 nm). The refined lattice parameters (*a*, *b*, and *c*) were 3.783, 3.783, and 9.512, and 3.785, 3.785, and 9.514 Å for NHTA and NTA, respectively. The calculated crystal cell volumes of NHTA and NTA were 136.13 and 136.30 Å^3, respectively. The lattice parameters of NHTA were slightly smaller than that of NTA, suggesting that the hydrogenation treatment resulted in distortion of the structures in NHTA even though hydrogenation did not change the anatase phase.

Raman spectroscopy is a more sensitive technique than XRD for monitoring the variation of the microstructure.[32] As shown in Figure 1 B, both samples possess five Raman vibration peaks located at approximately 149, 202, 403, 513, and 639 cm^{-1} (Figure 1 B), which were ascribed to E_g, E_g, B_{1g}, A_{1g} (B_{1g}), and E_g characteristic vibration modes of anatase, the dominant

phase.[29] The Raman peaks of NHTA shifted significantly, and weakened and broadened compared with those of NTA, which indicated that hydrogenation changed the geometric symmetry of NTA as a result of distortion of the structure. This agreed with the XRD results and previous reports.[26, 33]

The SEM image (Figure 2 A) shows that the NHTA sample had a flower-like hierarchical architecture composed of a number of nanoplates aligned at certain angles. The high-resolution SEM (Figure 2 B) shows that the average diameter of the constituent nanoplates is approximately 500 nm and that
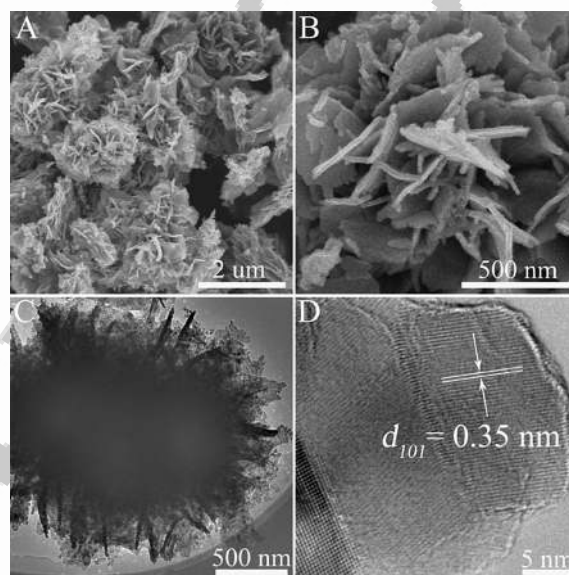

Figure 2. (A, B) SEM, (C) TEM, and (D) high-resolution TEM images of the NHTA material.

they have an almost uniform thickness of approximately 10 nm. AFM (Figure S1, Supporting Information) characterization further confirmed that the thickness of a typical nanoplate was approximately 10 nm. The TEM image (Figure 2 C) of NHTA confirmed the flower-like morphology of the angularly aggregated NTA nanoplates. The high-resolution TEM in Figure 2 D clearly shows the lattice fringes with a d-spacing of approximately 0.35 nm, which corresponds to the (101) crystal surface of anatase. More importantly, a single TiO$_2$ crystal nanoplate was surrounded by an ultrathin disordered layer, which was not observed in the NTA sample (Figure S2). The results suggest the disordered surrounding layer on NHTA nanoplates was caused by hydrogenation, in good agreement with the disordered structure of hydrogenated TiO$_2$.[26] The assembly and microstructure of NTA are very similar to that of NHTA (Figure S3); both don't have nanoscale pores in the constituent nanoplates. Notably, only randomly aggregated TiO$_2$ nanoparticles were obtained through the same synthesis procedure in the absence of tripolycyanamide (Figure S4). Apparently, in addition to acting as a N source (see below), tripolycyanamide plays an essential role in the formation of a hierarchical structure.

Room temperature EPR measurements were used to investigate the Ti^{3+} and oxygen vacancies (O$_{vac}$).[34] A broad and re-

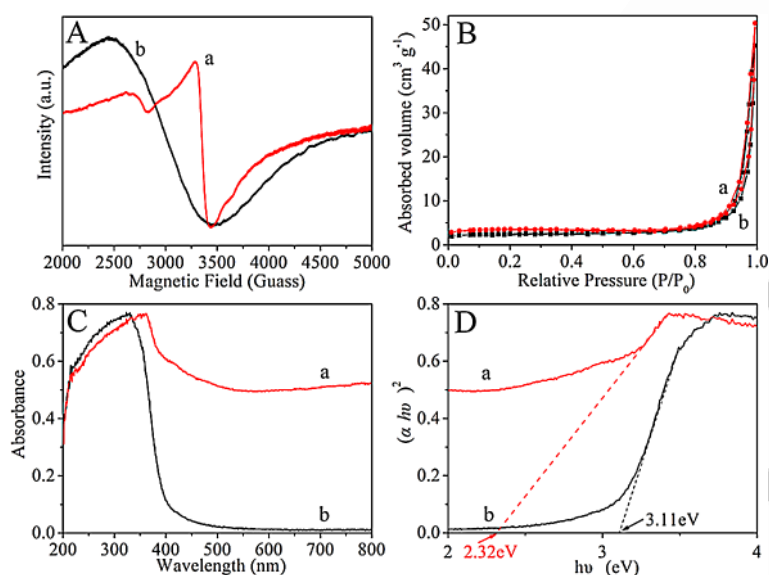↖↖ **These are not the final page numbers!**

Figure 3. (A) The EPR profiles, (B) N_2 adsorption–desorption isotherms, (C) UV/Vis diffuse reflectance spectra, and the (D) Tauc plots of (a) NHTA and (b) NTA.

markable EPR resonance at low-field with a "g" factor of 2.097 was observed (Figure 3 A), which was attributed to the active oxygen species sitting on the O_{vac}.[17,35] However, the asymmetric resonance, peculiarly at a higher field, implies the presence of Ti^{3+} ($g \approx 1.97$) or Ti cations with a lower valence state, which is caused by the hydrogenation treatment and is essential to maintain the neutral charge of the deficient NHTA.[36] However, only a small amount of Ti^{3+} species was identified by X-ray photoelectron spectroscopy (XPS), indicating that Ti^{3+} mainly exist in the bulk because the Ti^{3+} species are not stable on the surface and easily oxidized in air.[34] The above analysis indicates that the Ti^{3+} exists in the bulk of NHTA and O_{vac} dominate the disordered NHTA surface.[37]

Narrow hysteresis loops are observed at a high relative pressure in the N_2 adsorption–desorption isotherms of NHTA and NTA (Figure 3 B), indicating that NHTA and NTA contain large pores[27,38] with mean diameters of approximately 42 and 50 nm, respectively (Figure S5). These large pores result from interstices between the nanoplates. The specific surface areas (SSAs) of NHTA and NTA were 12.2 and 8.6 $m^2 g^{-1}$, respectively, suggesting that the hydrogenation treatment increases the SSA.

Band structure and optical properties

The UV/Vis diffuse reflectance spectra (UV/Vis-DRS, Figure 3 C) prove that the N doping can extend the light absorption of TiO_2 from the UV to the visible region (up to 500 nm for NTA), whereas NHTA can even absorb light energy in the whole visible region (Figure S6). The significant absorption of NHTA in the visible light region can be assigned to the impurity midgaps induced by N and H doping.[2] The corresponding bandgap deduced from Tauc plots (Figure 3 D) of NHTA ($E_g = 2.32$ eV) was 0.79 and 0.88 eV

smaller than the bandgap energies of NTA (3.11 eV) and pristine anatase (3.2 eV). Apparently, hydrogenation plays a more significant role than N doping in narrowing the bandgap of TiO_2. Even though the narrowing of the bandgap was more significant in our case compared with reported N/H-codoped TiO_2, we could not evaluate if there was synergism between N doping and hydrogenation in our NHTA sample, which has previously been reported in the literature,[2,19] because samples derived from this method always contained nitrogen. Spectral and photoelectrochemical characterization were used to investigate the origin of the bandgap narrowing.

XPS was used to investigate the surface chemical composition and valence band maximum (VBM) potentials of the samples. The core-level Ti 2p XPS (Figure 4 A) peaks of NHTA and
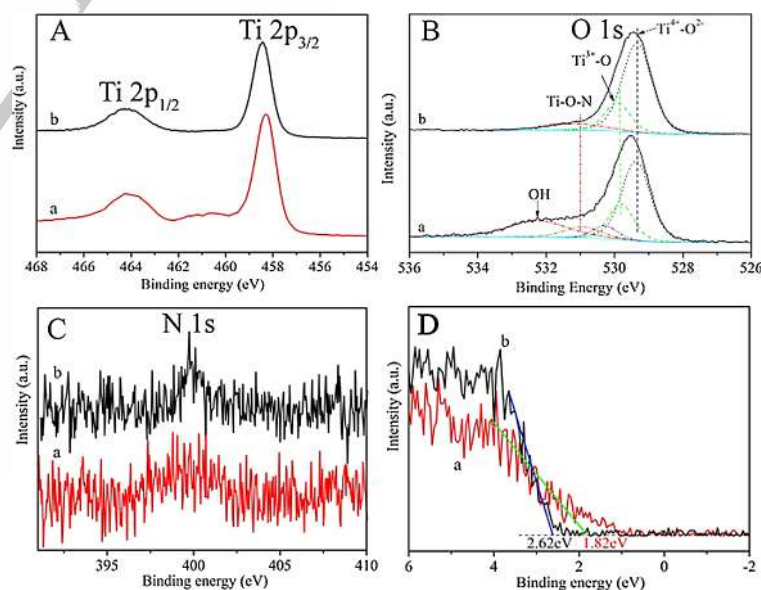

Figure 4. XPS for (A) Ti 2p, (B) O 1s, (C) N 1s and (D) valence band spectra of (a) NHTA and (b) NTA.

These are not the final page numbers! ↗↗

NTA had the same shape but a different intensity. The Ti $2p_{3/2}$ peaks centered at approximately 458.3 and 464.5 eV were ascribed to Ti^{4+} of TiO_2.[39] The slightly asymmetric Ti 2p XPS peaks (with lower binding energy) of the samples indicated that there was a very small amount of Ti^{3+} ions at the surfaces of NHTA and NTA. The Ti $2p_{3/2}$ XPS peaks were difficult to fit to determine the amount of low valance Ti cations, whereas the fitting of the O 1s XPS peaks indicated that the NHTA had a higher Ti^{3+}/Ti^{4+} ratio than that of NTA. The XPS shake-up peak located between Ti $2p_{1/2}$ and Ti $2p_{3/2}$, which was absent in NTA, ■■ok?■■ could be attributed to deep, reduced Ti cations ($Ti^{3-\delta}$, $\delta > 0$).[40]

The O 1s XPS for NHTA was distinct from that of NTA, as shown in Figure 4B. The strongest O 1s XPS peaks of both samples were observed between 531 and 528 eV, which were asymmetric and could be fitted into two peaks attributed to O—Ti^{IV} (≈ 529.4 eV) and Ti^{III}—O (≈ 529.9 eV) bonds. The area ratios of the O—Ti^{IV} and O—Ti^{III} peaks for NHTA and NTA were 2.19 and 3.11, respectively, suggesting that NHTA had much more O_{vac} than NTA. An extra O_{vac} peak could be deconvoluted from the O 1s XPS peak of NHTA at 530.9 eV, which was attributed to the —OH group stabilized O_{vac}. A Ti—OH bond was observed at 532.2 eV (Figure 4 B) exclusively for NHTA.[28,41] ■■ok?■■

Both NTA and NHTA displayed very similar O 1s XPS peaks at 531 eV, which was attributed to the TiO—N bond.[17] The very similar N 1s XPS spectra in Figure 4C shows further evidence that the nitrogen atoms localized in TiO—N bonds (≈ 400 eV).[17,42] ■■ok?■■The N-doping levels were determined to be approximately 1 wt% in NTA and 0.8 wt% in NHTA. The N doping was attributed to the thermal decomposition of tripolycyanamide; the post-hydrogenation slightly reduced the N-doping concentration. The residual carbon species were removed thoroughly according to the results of C 1s XPS (Figure S7) and thermogravimetric analysis (TGA) (Figure S8). No further weight loss was observed in the TGA profiles at calcination temperatures above 600 °C.

As shown in the valence band (VB) XPS (Figure 4D), the VBM of NHTA was located at 1.82 eV, which was 0.8 eV and 1.18 eV lower than the VBM of NTA (2.62 eV) and TiO_2 (3.0 eV), respectively.[43] Accordingly, the conductance band minima (CBM) of NHTA and NTA were −0.50 and −0.49 eV, respectively, as calculated by CBM = VBM − E_g. The results suggest that hydrogenation significantly decreases the VBM but slightly decreases the CBM. ■■ok?■■Previously reported density functional theory simulations and experimental results of N-doped TiO_2 qualitatively suggest that O_{vac} can increase the VBM ■■ok?■■ and Ti^{3+} (3 d orbitals) can change the CBM, which depends on the amount of Ti^{3+}.[16,17,41,44,45] The almost similar CBM for the NHTA and NTA suggested that the total amount of $Ti^{3-\delta}$ was rather low, consistent with the core-level XPS analyses.

According to the above UV/Vis and XPS spectral analyses, the energetic band structure diagrams of the modified TiO_2 are illustrated in Figure 5. Compared to pristine TiO_2, the N doping shifts the VBM by approximately 0.38 eV, whereas the hydrogenation treatment further decreases the VBM by 0.80 eV, indicating that the hydrogenation contributes more than N doping to
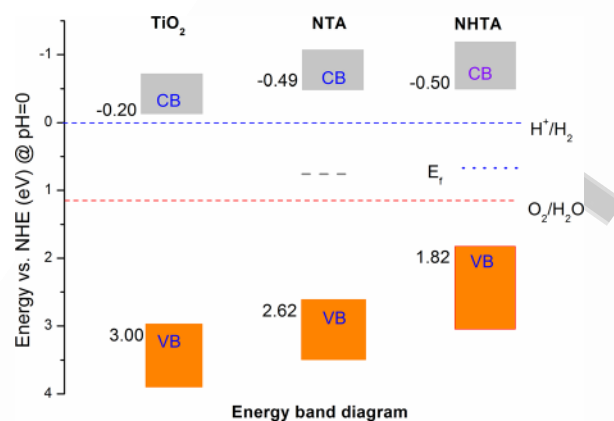

Figure 5. Energy band diagrams of TiO_2, NTA, and NHTA.

the change in the VB. The VBM energies of the samples are all more positive than the O_2/H_2O potential, allowing them to oxidize water, and NTA and NHTA are more active than TiO_2 for the evolution of H_2 because of their more negative CBM energies. The very similar CBM potentials of NTA and NHTA imply that they should have the same "power" to reduce protons, but the NHTA had much higher reactivity. Therefore, there are other factors besides the revised band structure of NHTA that contribute to its enhanced H_2 evolution (see below).

Scanning Kelvin probe microscopy (SKPM) ■■ok?■■ can be used to measure the flat potential or Fermi level according to the work function.[46] The measured work functions of NHTA and NTA (Figure 6) were 5.17 and 5.26 eV, respectively. The smaller work function of NHTA indicates that it possesses a more negative Fermi level or flat band than NTA, namely, the valance electrons are much easier to be excited and transfer to the adjacent co-catalysts, which favors photocatalytic hydrogen evolution.
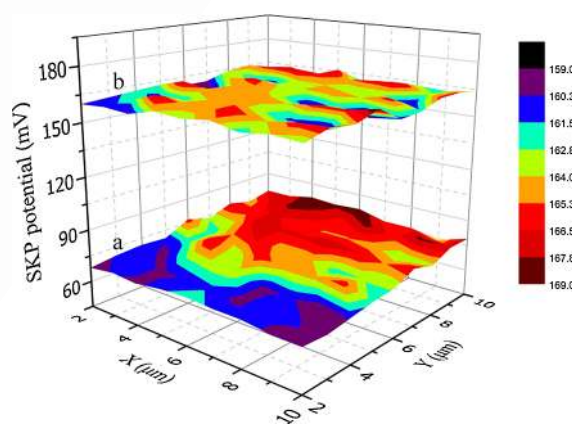

Figure 6. SKPM maps of (a) NHTA and (b) NTA.

Photocatalytic H_2 evolution and photoelectric properties

Under 3 h AM 1.5 irradiation, the mean photocatalytic hydrogen evolution on NHTA was approximately 1500 µmol g^{-1} h^{-1}, superior to that on NTA (≈ 690 µmol g^{-1} h^{-1}, Figure 7 A) and

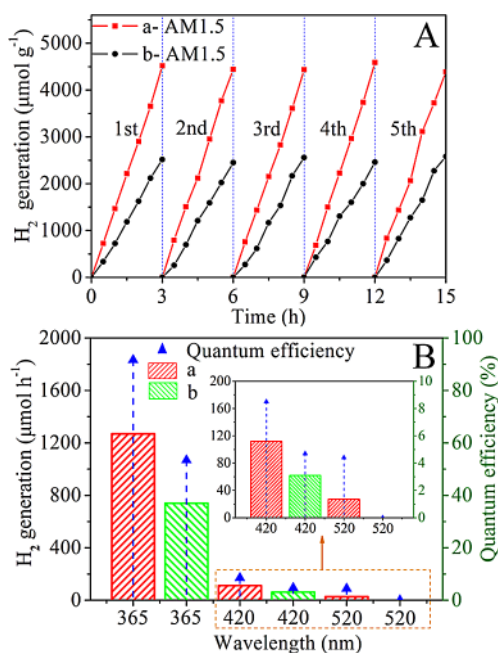↗↗ **These are not the final page numbers!**

Figure 7. (A, B) Photocatalytic hydrogen evolution of (a) NHTA and (b) NTA. (A) Cycling tests of photocatalytic hydrogen generation under AM 1.5. (B) The photocatalytic hydrogen evolution rates under single-wavelength light and the corresponding QE. The inset is an enlargement of the 420–520 nm region.

those reported in the literature (Table S1). The highly active NHTA was stable and resistant to photodegradation during the photocatalytic hydrogen evolution as there was no decrease in activity observed after five recycling tests (Figure 7 A). It is important to investigate the H_2 evolution of the flower-like photocatalysts under different light irradiation because more visible-light-responsive photocatalysts are less active under UV. As compared in Figure 7 B, the H_2 evolution rate on NHTA under UV (365 nm) was approximately 1280 µmol g^{-1}h^{-1}, ■■ok?■■ much higher than those under 420 nm (110 µmol g^{-1}h^{-1}) and 520 nm (30 µmol g^{-1}h^{-1}) visible-light illumination.

The apparent quantum efficiencies (QEs) were calculated to evaluate the solar energy conversion ability of the materials using Equation (1):

$$QE = \frac{2 \times (\text{number of evolved } H_2 \text{ molecules})}{(\text{number of incident photons})} \times 100\%$$
(1)

The QEs of NHTA and NTA were 92 and 58%, respectively, under UV light irradiation at 365 nm. However, the QEs of NHTA illuminated with visible light at 420 and 520 nm were only 9 and 5%, respectively. The QE of NTA was only approximately 6% at 420 nm and negligible at 520 nm. Therefore, the hydrogenation of NTA enhanced the H_2 evolution in visible light owing to the greatly extended absorption in the long-wavelength region, but the promotion is insignificant in terms of QE. Moreover, without Pt as a co-catalyst, the NHTA materi-

als still showed a superior photocatalytic performance compared with NTA materials, even though both the hydrogen production rates were extremely low (Figure S9).

The fate of the photogenerated charge carriers

The above reaction results confirm that UV light is still much more efficient than visible light for the reduction of protons on NHTA and NTA. A higher H_2 evolution under full arc illumination results under UV irradiation, whereas there were no significant differences in UV absorption for NTA and NHTA samples. The origin of the different photocatalytic efficiency between NHTA and NTA still remained unresolved. We used surface photovoltage spectroscopy (SPS), photoluminescence (PL), and photoelectrochemical spectra to determine the fates of the photogenerated excitons. ■■ok?■■

The surface photovoltaic spectral response maxima of NTA and NHTA at 350 nm (SPS, Figure 8 A), but their SPS intensity ratio was approximately 8.3 ($I_{NHTA}/I_{NTA} = 8.3$), suggesting that NHTA had a higher carrier separation efficiency because hydrogenation dramatically improved the charge carrier separation ability of NHTA.[41] ■■ok?■■The SPS onset of NHTA was also redshifted to approximately 425 nm in comparison to that of NTA owing to its absorption in the visible light region (see UV/Vis spectra). The SPS response in the broader visible light range was negligible, suggesting that the majority of the charge carriers excited by visible light could not be effectively separated or were prone to recombination before reducing to protons.
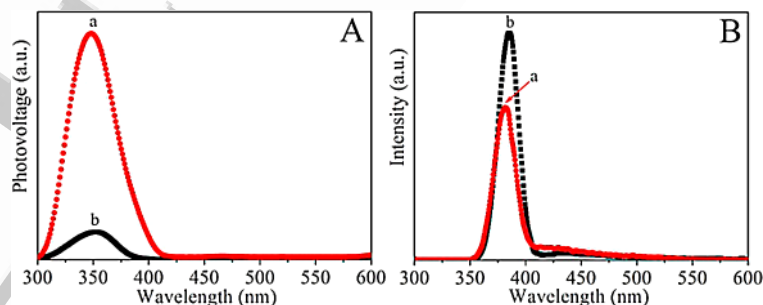

Figure 8. (A) Surface photovoltage spectroscopy and (B) photoluminescence of (a) NHTA and (b) NTA.

The PL intensity is relevant to the recombination of photogenerated charge carriers.[47] Figure 8 B shows that the fluorescence intensity of NHTA was lower than that of NTA ($I_{NHTA}/I_{NTA} = 1:1.49$) in the UV region, suggesting that less UV-excited charge carriers are recombined in NHTA compared to NTA.[48, 49] Stronger fluoresce emission was observed for NHTA relative to NTA in the 400–500 nm region, indicating more visible-light-excited charge carriers are recombined in NHTA despite the stronger absorption of visible light.

Moreover, the maximum PL responses were located at different wavelengths, suggesting that there was a certain surface state that traps the photogenerated electrons of the n-type NHTA and NTA.[2] Both the SPS and PL results clearly suggest

that NHTA would be superior to NTA in photocatalytic hydrogen production because of stronger light harvesting, higher charge separation, and less recombination in the UV region, despite stronger recombination of excitons in the visible light region. Nevertheless, PL and photoelectrochemical characterization could not explain the enhanced charge separation of NHTA with smaller E_g because this is usually associated with a lower separation force and faster recombination. ■■ok?■■ ■

The linear voltammetry sweeps in dark and under the same irradiation conditions are presented in Figure 9A. It shows that the dark current density on the NTA and NHTA was almost the same within a broad applied bias range. Under the simulated AM 1.5 illumination and zero applied bias versus Ag/AgCl, the NHTA electrode shows a photocurrent density (J_C) 15 μA cm^{-2} greater than that of the NTA electrode. Figure 9B displays the transient chronoamperometry of the samples collected at 0.4 V applied bias. Both NHTA and NTA display prompt and constant on–off responses under AM 1.5 irradiation, although the J_C of NHTA was approximately 18 μA cm^{-2}, 3.6 times higher than that of the NTA photoelectrode (5 μA cm^{-2}).

The electrochemical impedance spectra (EIS) of the specimens were collected in 1 M KOH aqueous solution and are shown in Figure 9C and D. Compared to NTA, the NHTA electrode showed smaller hemicycles in the Nyquist plot (Figure 9C), which indicated that the NHTA was more resistant to charge recombination, namely, it had a higher charge mobility than NTA. The resistance becomes more significant under AM 1.5 illumination than in the dark, suggesting that the interface resistance decreases owing to the accumulation of photoelectrons at the interface. The Nyquist results indicate that NHTA was more efficient than NTA in charge carrier separation and transportation, which was consistent with the SPS analysis.

Positive slopes were observed in the Mott–Schottky plots, as shown in Figure 9D, confirming that they are n-type semiconductors.[49] The smaller slope of NHTA (1.01×10^{-10}) compared with that of NTA (2.24×10^{-10}) suggested that NHTA had a higher donor density (N_d), according to literature and the following Equation (2):[45, 50]

$$N_d = \frac{2/e_0 \varepsilon \varepsilon_0}{\mathrm{d}(1/C^2)/\mathrm{d}V} \tag{2}$$

where N_d is carrier density, e_0 is the electron charge, ε is the dielectric constant of TiO$_2$, and ε_0 is the permittivity of vacuum. Taking the dielectric coefficient as 55 for anatase, the calculated N_d of NHTA and NTA were 2.4×10^{18} and 1.1×10^{18} cm^{-3}, respectively. The richer donor density in NHTA is owing to the presence of Ti$^{3-\delta}$ and O$_{vac}$ in the bulk and the disordered surface of the NHTA nanoplates, which favors the photocatalytic H$_2$ evolution and enhanced the photoelectrochemical performance of NHTA.

Retrieved from the Mott–Schottky plots, the flat band energies (E_{fb}) of NHTA and NTA were −0.89 and −0.78 eV versus Ag/AgCl [$E_{Ag/AgCl}$ is $\approx$0.198 eV vs. NHE (normal hydrogen electrode) at pH 6.5], respectively. Because the Mott–Schottky test was performed at room temperature, the room temperature compensation potential was approximately 25 meV versus NHE, and the Fermi levels of the NHTA and NTA were calculated as −0.67 and −0.56 eV versus NHE (meaning 0.67 and 0.56 eV in the energy diagram), respectively. The results are consistent with the VB, XPS, and SKPM characterization.

Conclusions

A facile two-step strategy was used to prepare black N/H-TiO$_2$ nanoplates with flower-like hierarchical architectures, in which tripolycyanamide was used as both an assembly directing-agent and N source in the first hydrothermal synthesis stage, and the subsequent hydrogen reduction not only introduced
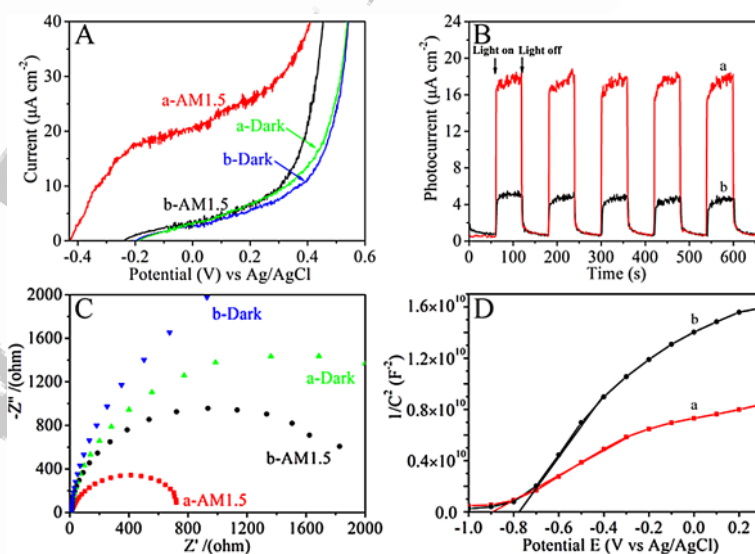
Figure 9. Photoelectrochemical properties of (a) NHTA and (b) NTA: (A) linear sweep voltammograms under dark and AM 1.5 illumination, (B) the chronoamperometry waveform ■■ok?■■■ at 0.4 V energy bias, (C) the Nyquist plots of electrochemical impedance under dark and AM 1.5 illumination, and (D) the Mott–Schottky plots acquired at 1000 Hz.

↖↖ These are not the final page numbers!

hydroxyl groups but also created a high concentration of oxygen vacancies and a small amount of $Ti^{3-\delta}$ cations in the anatase. The hydrogenation played a more major role than N doping in narrowing the bandgap of TiO_2.

The obtained NHTA nanoarchitecture exhibited enhanced photoelectrochemical responses and excellent photocatalytic hydrogen evolution under UV and visible light. The average photocatalytic hydrogen generation rate on NHTA was approximately 1500 $\mu mol\,g^{-1}h^{-1}$ under AM 1.5 irradiation, two times that of NTA ($\approx 690\;\mu mol\,g^{-1}h^{-1}$). However, visible light was still much less effective than UV for the photocatalytic H_2 evolution on NHTA and NTA.

By combining the explicit band structure, photoelectric, and photoelectrochemical analysis using UV/Vis diffuse reflectance spectroscopy, X-ray photoelectron spectroscopy, scanning Kelvin probe microscopy, surface photovoltage spectroscopy, photoluminescence, and electrochemical impedance spectroscopy characterization techniques, the superior performance of NHTA compared with NTA for the photocatalytic H_2 evolution could be reasonably attributed to the synergistic effects of enhanced light absorption owing to a narrower bandgap, effective charge carrier separation and transportation, and suppressed charge recombination.

Experimental Section

Materials and preparation

Tetrabutyl titanate $[Ti(OC_4H_9)_4]$, tripolycyanamide $(C_3H_6N_6,$ CAS number 108-78-1) and methanol were used as received without further purification. All chemicals were of analytical grade and purchased from Aladdin Reagent Corp. In a typical experimental procedure, 1.7 g of $Ti(OC_4H_9)_4$ was added dropwise into 30 mL of methanol under vigorous stirring for 30 min, followed by the addition of 1.26 g tripolycyanamide under rigorous magnetic stirring (2 h) and subsequent ultrasonication (20 min). The milky white suspension was transferred into a 50 mL Teflon-lined stainless-steel autoclave and heated statically at 180 °C for 12 h in an electric oven. After cooling to room temperature naturally, the product was collected and washed with ethanol by centrifugation to remove impurities before drying at 60 °C for 3 h. The dry gel was then calcined at 600 °C for 4 h to obtain the flower-like hierarchical N-doped TiO_2 anatase (denoted as NTA). The as-prepared NTA product was further hydrogenated at 600 °C in a continuous H_2 flow (100 mL min^{-1}) for 3 h to obtain flower-like N-doped black anatase TiO_2 (NHTA).

Characterization

XRD patterns were recorded on Bruker D8 Discover diffractometer, with CuK$_\alpha$ radiation ($\lambda = 1.5406$ Å) within $2\theta = 20-60°$. SEM images were obtained using a Hitachi S-4800 instrument with an accelerating voltage of 15 kV. The SEM specimens were dispersed and fixed on a conducting resin. The TEM and HRTEM images of the sample were obtained on a JOEL JEM 2100F operated at an accelerating voltage of 200 kV. Raman spectra were acquired using a Jobin Yvon HR 800 micro-Raman spectrometer with an excitation laser wavelength of 457.9 nm on the surface of the sample. The BET surface areas of the samples were calculated from adsorption isotherm data using a multi-station high-speed gas sorption analyzer

(NOVA3000). The EPR (X-band) spectrum was measured at room temperature on a JES-FA 300 EPR spectrometer applying 1 mW microwave. XPS was performed on an ULTRA AXIS DLD with AlK$_\alpha$ (1253.6 eV) as the achromatic X-ray source, and the binding energy was calibrated by setting the C 1s peak to 285 eV. The diffuse reflectance spectra of the samples were recorded on a Shimadzu UV/ Vis spectrophotometer (UV 2550). SKPM ■■ok?■■ measurements were determined using a SKP5050 system. A Au electrode was used as a reference electrode, and the working electrode was prepared by traditional spray coating method on transparent conducting glass (FTO). The SPS measurements were performed with a home-built apparatus (excitation wavelength of 355 nm). The PL spectra of the samples were detected on a PE LS 55 spectrofluorophotometer at an excitation wavelength of 325 nm.

Photocatalysis

100 mg of as-prepared photocatalysts was taken into a home-made reactor containing 80 mL deionized water and 20 mL methanol. $H_2PtCl_6\cdot6H_2O$ (0.5 wt % to NHTA or NTA) was added as a co-catalyst. Before photocatalytic testing, the reactor and the entire gas-circulating system were de-aerated using a vacuum pump for 30 min. All photocatalytic hydrogen generation tests were under continuous illumination of an Autolight CEL-HXF300 xenon lamp (300 W) equipped with optical cut-off filters to realize AM 1.5 and monochromatic wavelengths of 365, 420, and 520 nm. The photocatalytic H_2 production was determined by Agilent gas chromatography (GC, 7900) at the same sampling time intervals.

Photoelectrochemical measurements

The photoelectrochemical performance was tested on Princeton VersaSTAT under AM 1.5 illumination in a home-made conventional three-electrode system reactor containing 1 M KOH electrolyte solution as well as a Pt foil counter electrode and an Ag/AgCl reference electrode. The working electrode was coated with as-prepared NHTA or NTA using spray pyrolysis onto the conductive FTO glass in an effective area of 1 cm^2. 0.2 g of the powder was dispersed into 4 mL ethanol and sonicated for 15 min, and then spattered onto the FTO substrate under a constant temperature of 80 °C, and finally calcined at 300 °C for 1 h under N_2 to firm the films. The chronoamperometry waveforms ■■ok?■■measured at 0.4 V versus Ag/AgCl electrode in 660 seconds and electrochemical impedance spectra were recorded at 10 mV oscillation amplitude in the frequency range of 0.05 Hz to 10 kHz.

Acknowledgements

[1] M. Fujihira, Y. Satoh, T. Osa, *Nature* **1981**, *293*, 206–208.

These are not the final page numbers! ↗↗

[2] X. Chen, S. Shen, L. Guo, S. S. Mao, *Chem. Rev.* **2010**, *110*, 6503–6570.

[3] H. B. Kim, H. Kim, W. I. Lee, D. J. Jang, *J. Mater. Chem. A* **2015**, *3*, 9714–9721.

[4] W. Li, Z. Wu, J. Wang, A. A. Elzatahry, D. Zhao, *Chem. Mater.* **2014**, *26*, 287–298.

[5] X. Li, J. Wang, Y. Men, Z. Bian, *Appl. Catal. B* **2016**, *187*, 115–121.

[6] Z. Jiang, W. Wei, D. Mao, C. Chen, Y. Shi, X. Lv, J. Xie, *Nanoscale* **2015**, *7*, 784–797.

[7] W. Zhou, H. Fu, *ChemCatChem* **2013**, *5*, 885–894.

[8] X. Chen, Z. Zhang, L. Chi, A. K. Nair, W. Shangguan, Z. Jiang, *Nano-Micro Lett.* **2016**, *8*, 1–12.

[9] Y. Zhang, W. Zhu, X. Cui, W. Yao, T. Duan, *CrystEngComm* **2015**, *17*, 8368–8376.

[10] M. O. Ansari, M. M. Khan, S. A. Ansari, M. H. Cho, *New J. Chem.* **2015**, *39*, 8381–8388.

[11] R. Reichert, Z. Jusys, R. J. Behm, *J. Phys. Chem. C* **2015**, *119*, 24750–24759.

[12] W. Zhu, S. Xiao, D. Zhang, P. Liu, H. Zhou, W. Dai, F. Liu, H. Li, *Langmuir* **2015**, *31*, 10822–10830.

[13] J. Zhang, Y. Wu, M. Xing, S. A. K. Leghari, S. Sajjad, *Energy Environ. Sci.* **2010**, *3*, 715–726.

[14] S. Pany, K. M. Parida, *ACS Sustainable Chem. Eng.* **2014**, *2*, 1429–1438.

[15] L. Lo Presti, M. Ceotto, F. Spadavecchia, G. Cappelletti, D. Meroni, R. G. Acres, S. Ardizzone, *J. Phys. Chem. C* **2014**, *118*, 4797–4807.

[16] Z. Jiang, F. Yang, N. Luo, B. T. Chu, D. Sun, H. Shi, T. Xiao, P. P. Edwards, *Chem. Commun.* **2008**, 6372–6374.

[17] Z. Jiang, L. Kong, F. S. Alenazey, Y. Qian, L. France, T. Xiao, P. P. Edwards, *Nanoscale* **2013**, *5*, 5396–5402.

[18] G. Yang, Z. Jiang, H. Shi, T. Xiao, Z. Yan, *J. Mater. Chem.* **2010**, *20*, 5301–5309.

[19] X. Chen, L. Liu, P. Y. Yu, S. S. Mao, *Science* **2011**, *331*, 746–750.

[20] M. Tian, M. Mahjouri-Samani, G. Eres, R. Sachan, M. Yoon, M. F. Chisholm, K. Wang, A. A. Puretzky, C. M. Rouleau, D. B. Geohegan, G. Duscher, *ACS Nano* **2015**, *9*, 10482–10488.

[21] A. Naldoni, M. Allieta, S. Santangelo, M. Marelli, F. Fabbri, S. Cappelli, C. L. Bianchi, R. Psaro, V. Dal Santo, *J. Am. Chem. Soc.* **2012**, *134*, 7600–7603.

[22] L. Xin, X. Liu, *RSC Adv.* **2015**, *5*, 71547–71550.

[23] T. Xia, X. Chen, *J. Mater. Chem. A* **2013**, *1*, 2983–2989.

[24] H. Cui, W. Zhao, C. Yang, H. Yin, T. Lin, Y. Shan, Y. Xie, H. Gu, F. Huang, *J. Mater. Chem. A* **2014**, *2*, 8612–8616.

[25] J. Dong, J. Han, Y. Liu, A. Nakajima, S. Matsushita, S. Wei, W. Gao, *ACS Appl. Mater. Interfaces* **2014**, *6*, 1385–1388.

[26] W. Zhou, W. Li, J.-Q. Wang, Y. Qu, Y. Yang, Y. Xie, K. Zhang, L. Wang, H. Fu, D. Zhao, *J. Am. Chem. Soc.* **2014**, *136*, 9280–9283.

[27] W. Zhou, F. Sun, K. Pan, G. Tian, B. Jiang, Z. Ren, C. Tian, H. Fu, *Adv. Funct. Mater.* **2011**, *21*, 1922–1930.

[28] X. Chen, L. Liu, F. Huang, *Chem. Soc. Rev.* **2015**, *44*, 1861–1885.

[29] F. Tian, Y. Zhang, J. Zhang, C. Pan, *J. Phys. Chem. C* **2012**, *116*, 7515–7519.

[30] H. G. Yang, C. H. Sun, S. Z. Qiao, J. Zou, G. Liu, S. C. Smith, H. M. Cheng, G. Q. Lu, *Nature* **2008**, *453*, 638–641.

[31] L. Wang, T. Sasaki, *Chem. Rev.* **2014**, *114*, 9455–9486.

[32] Y. Zhang, C. X. Harris, P. Wallenmeyer, J. Murowchick, X. Chen, *J. Phys. Chem. C* **2013**, *117*, 24015–24022.

[33] C. Yang, Z. Wang, T. Lin, H. Yin, X. Lü, D. Wan, T. Xu, C. Zheng, J. Lin, F. Huang, X. Xie, M. Jiang, *J. Am. Chem. Soc.* **2013**, *135*, 17831–17838.

[34] N. Liu, C. Schneider, D. Freitag, M. Hartmann, U. Venkatesan, J. Müller, E. Spiecker, P. Schmuki, *Nano Lett.* **2014**, *14*, 3309–3313.

[35] X. Wang, Y. Yan, B. Hao, G. Chen, *Dalton Trans.* **2014**, *43*, 14054–14060.

[36] A. Lepcha, C. Maccato, A. Mettenbörger, T. Andreu, L. Mayrhofer, M. Walter, S. Olthof, T. P. Ruoko, A. Klein, M. Moseler, K. Meerholz, J. R. Morante, D. Barreca, S. Mathur, *J. Phys. Chem. C* **2015**, *119*, 18835–18842.

[37] Q. Kang, J. Cao, Y. Zhang, L. Liu, H. Xu, J. Ye, *J. Mater. Chem. A* **2013**, *1*, 5766–5774.

[38] J. G. Yu, Y. R. Su, B. Cheng, *Adv. Funct. Mater.* **2007**, *17*, 1984–1990.

[39] Z. Song, J. Hrbek, R. Osgood, *Nano Lett.* **2005**, *5*, 1327–1332.

[40] T. Hanawa, *J. Periodontal Implant Sci.* **2011**, *41*, 263–272.

[41] A. S. Alshammari, L. Chi, X. Chen, A. Bagabas, D. Kramer, A. Alromaeh, Z. Jiang, *RSC Adv.* **2015**, *5*, 27690–27698.

[42] F. Zou, Z. Jiang, X. Qin, Y. Zhao, L. Jiang, J. Zhi, T. Xiao, P. P. Edwards, *Chem. Commun.* **2012**, *48*, 8514–8516.

[43] W. Zhao, Y. Li, M. Zhang, J. Chen, L. Xie, Q. Shi, X. Zhu, *Chem. Eng. J.* **2016**, *283*, 105–113.

[44] S. Banerjee, S. C. Pillai, P. Falaras, K. E. O'Shea, J. A. Byrne, D. D. Dionysiou, *J. Phys. Chem. Lett.* **2014**, *5*, 2543–2554.

[45] C. Mao, F. Zuo, Y. Hou, X. Bu, P. Feng, *Angew. Chem. Int. Ed.* **2014**, *53*, 10485–10489; *Angew. Chem.* **2014**, *126*, 10653–10657.

[46] S. U. Nanayakkara, G. Cohen, C.-S. Jiang, M. J. Romero, K. Maturova, M. Al-Jassim, J. van de Lagemaat, Y. Rosenwaks, J. M. Luther, *Nano Lett.* **2013**, *13*, 1278–1284.

[47] J. Hu, J. Jiang, L. Wu, K. Xu, X. Hou, Y. Lv, *Anal. Chem.* **2011**, *83*, 6552–6558.

[48] I. Mora-Seró, T. Dittrich, A. Belaidi, G. Garcia-Belmonte, J. Bisquert, *J. Phys. Chem. B* **2005**, *109*, 14932–14938.

[49] R. O'Hayre, M. Nanu, J. Schoonman, A. Goossens, *J. Phys. Chem. C* **2007**, *111*, 4809–4814.

[50] D. J. Wineland, *Angew. Chem. Int. Ed.* **2013**, *52*, 10179–10189; *Angew. Chem.* **2013**, *125*, 10367–10378.

↖↖ These are not the final page numbers!

FULL PAPERS

Stop and smell the nanoplates: Black N/H-TiO$_2$ nanoplates (NHTA) with a flower-like hierarchical architecture were fabricated using a two-step synthesis. The black NHTA achieved a photocatalytic hydrogen evolution rate of approximately 1500 µmol g^{-1} h^{-1} under AM 1.5 illumination. The band structure of the NHTA indicated the contribution of oxygen vacancies and the N dopant on the photocatalytic performance.

Energy band diagram
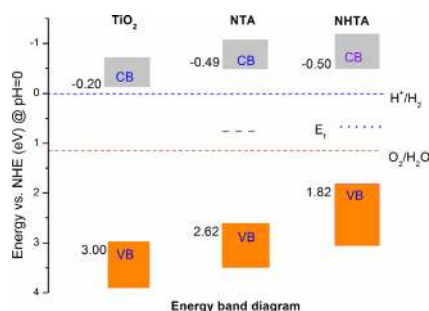
K. Zhang, W. Zhou,* L. Chi, X. Zhang, W. Hu, B. Jiang, K. Pan, G. Tian, Z. Jiang*

■■ – ■■

Black N/H-TiO$_2$ Nanoplates with a Flower-Like Hierarchical Architecture for Photocatalytic Hydrogen Evolution

Highly efficient #photocatalytic #hydrogenevolution using Ni/H-TiO$_2$ nanoplates SPACE RESERVED FOR IMAGE AND LINK

Share your work on social media! *ChemSusChem* has added Twitter as a means to promote your article. Twitter is an online microblogging service that enables its users to send and read text-based messages of up to 140 characters, known as "tweets". Please check the pre-written tweet in the galley proofs for accuracy. Should you or your institute have a Twitter account, please let us know the appropriate username (i.e., @accountname), and we will do our best to include this information in the tweet. This tweet will be posted to the journal's Twitter account @ChemSusChem (follow us!) upon online publication of your article, and we recommended you to repost ("retweet") it to alert other researchers about your publication.

Please check that the ORCID identifiers listed below are correct. We encourage all authors to provide an ORCID identifier for each coauthor. ORCID is a registry that provides researchers with a unique digital identifier. Some funding agencies recommend or even require the inclusion of ORCID IDs in all published articles, and authors should consult their funding agency guidelines for details. Registration is easy and free; for further information, see http://orcid.org/.

Kaifu Zhang
Prof. Wei Zhou
Lina Chi
Xiangcheng Zhang
Weiyao Hu
Baojiang Jiang
Kai Pan
Guohui Tian
Prof. Zheng Jiang

These are not the final page numbers! ↗↗